Authors
Giulia F Mancini, Robert M Karl, Elisabeth R Shanblatt, Charles S Bevis, Dennis F Gardner, Michael D Tanksalvala, Jennifer L Russell, Daniel E Adams, Henry C Kapteyn, John V Badding, Thomas E Mallouk, and Margaret M Murnane

Research Article | Vol. 26, No. 9 | 30 Apr 2018 | OPTICS EXPRESS 11393
Optics EXPRESS

Colloidal crystal order and structure revealed by tabletop extreme ultraviolet scattering and coherent diffractive imaging

GIULIA F. MANCINI,[1,7,8] ROBERT M. KARL JR.,[1,7,9] ELISABETH R. SHANBLATT,[1] CHARLES S. BEVIS,[1] DENNIS F. GARDNER,[1] MICHAEL D. TANKSALVALA,[1] JENNIFER L. RUSSELL,[2,3] DANIEL E. ADAMS,[1] HENRY C. KAPTEYN,[1] JOHN V. BADDING,[2,3,4,5] THOMAS E. MALLOUK,[2,3,4,6] AND MARGARET M. MURNANE[1]

[1]*JILA, University of Colorado, 440 UCB, Boulder, CO 80309-0440, USA*
[2]*Department of Chemistry, Penn State University, University Park, PA 16802, USA*
[3]*Materials Research Institute, Penn State University, University Park, PA 16802, USA*
[4]*Department of Physics, Penn State University, University Park, PA 16802, USA*
[5]*Department of Materials Science and Engineering, Penn State University, University Park, PA 16802, USA*
[6]*Department of Biochemistry and Molecular Biology, Penn State University, University Park, PA 16802, USA*
[7]*These authors contributed equally to this work*
[8]*giulia.mancini@colorado.edu*
[9]*robert.karl@colorado.edu*

Abstract: Colloidal crystals with specific electronic, optical, magnetic, vibrational properties, can be rationally designed by controlling fundamental parameters such as chemical composition, scale, periodicity and lattice symmetry. In particular, silica nanospheres -which assemble to form colloidal crystals- are ideal for this purpose, because of the ability to infiltrate their templates with semiconductors or metals. However characterization of these crystals is often limited to techniques such as grazing incidence small-angle scattering that provide only global structural information and also often require synchrotron sources. Here we demonstrate small-angle Bragg scattering from nanostructured materials using a tabletop-scale setup based on high-harmonic generation, to reveal important information about the local order of nanosphere grains, separated by grain boundaries and discontinuities. We also apply full-field quantitative ptychographic imaging to visualize the extended structure of a silica close-packed nanosphere multilayer, with thickness information encoded in the phase. These combined techniques allow us to simultaneously characterize the silica nanospheres size, their symmetry and distribution within single colloidal crystal grains, the local arrangement of nearest-neighbor grains, as well as to quantitatively determine the number of layers within the sample. Key to this advance is the good match between the high harmonic wavelength used (13.5nm) and the high transmission, high scattering efficiency, and low sample damage of the silica colloidal crystal at this wavelength. As a result, the relevant distances in the sample - namely, the interparticle distance (≈124nm) and the colloidal grains local arrangement (≈1μm) – can be investigated with Bragg coherent EUV scatterometry and ptychographic imaging within the same experiment simply by tuning the EUV spot size at the sample plane (5μm and 15μm respectively). In addition, the high spatial coherence of high harmonics light, combined with advances in imaging techniques, makes it possible to image near-periodic structures quantitatively and nondestructively, and enables the observation of the extended order of quasi-periodic colloidal crystals, with a spatial resolution better than 20nm. In the future, by harnessing the high time-resolution of tabletop high harmonics, this technique can be extended to dynamically image the three-dimensional electronic, magnetic, and transport properties of functional nanosystems.

#321043 https://doi.org/10.1364/OE.26.011393
Journal © 2018 Received 6 Feb 2018; revised 28 Mar 2018; accepted 3 Apr 2018; published 18 Apr 2018

Optics EXPRESS

OCIS codes: (340.7460) X-ray microscopy; (290.5820) Scattering measurements; (340.7480) X-rays, soft x-rays, extreme ultraviolet (EUV).

References and links

1. J. L. Russell, G. H. Noel, J. M. Warren, N.-L. L. Tran, and T. E. Mallouk, "Binary Colloidal Crystal Films Grown by Vertical Evaporation of Silica Nanoparticle Suspensions," Langmuir **33**(39), 10366–10373 (2017).
2. T. Li, A. J. Senesi, and B. Lee, "Small Angle X-ray Scattering for Nanoparticle Research," Chem. Rev. **116**(18), 11128–11180 (2016).
3. J. E. Han and V. H. Crespi, "Tuning Fermi-surface properties through quantum confinement in metallic metalattices: new metals from old atoms," Phys. Rev. Lett. **86**(4), 696–699 (2001).
4. J. E. Han and V. H. Crespi, "Abrupt Topological Transitions in the Hysteresis Curves of Ferromagnetic Metalattices," Phys. Rev. Lett. **89**(19), 197203 (2002).
5. M. J. Kosterlitz and D. J. Thouless, "Ordering, metastability and phase transitions in two-dimensional systems," J. Phys. Chem. **6**, 1181–1203 (1973).
6. M. T. Barako, A. Sood, C. Zhang, J. Wang, T. Kodama, M. Asheghi, X. Zheng, P. V. Braun, and K. E. Goodson, "Quasi-ballistic Electronic Thermal Conduction in Metal Inverse Opals," Nano Lett. **16**(4), 2754–2761 (2016).
7. M. A. Boles, M. Engel, and D. V. Talapin, "Self-Assembly of Colloidal Nanocrystals: From Intricate Structures to Functional Materials," Chem. Rev. **116**(18), 11220–11289 (2016).
8. J. Miao, T. Ishikawa, I. K. Robinson, and M. M. Murnane, "Beyond crystallography: Diffractive imaging using coherent x-ray light sources," Science **348**(6234), 530–535 (2015).
9. M. Altarelli, R. P. Kurta, and I. A. Vartanyants, "X-ray cross-correlation analysis and local symmetries of disordered systems: General theory," Phys. Rev. B **82**, 104207 (2010).
10. R. P. Kurta, M. Altarelli, E. Weckert, and I. A. Vartanyants, "X-ray cross-correlation analysis applied to disordered two-dimensional systems," Phys. Rev. B **85**, 184204 (2012).
11. P. Wochner, C. Gutt, T. Autenrieth, T. Demmer, V. Bugaev, A. D. Ortiz, A. Duri, F. Zontone, G. Grübel, and H. Dosch, "X-ray cross correlation analysis uncovers hidden local symmetries in disordered matter," Proc. Natl. Acad. Sci. U.S.A. **106**(28), 11511–11514 (2009).
12. P. Wochner, M. Castro-colin, S. N. Bogle, and V. N. Bugaev, "Of fluctuations and cross-correlations: finding order in disorder," Int. J. Mater. Res. **102**, 874–888 (2011).
13. F. Lehmkühler, B. Fischer, L. Müller, B. Ruta, and G. Grübel, "Structure beyond pair correlations: X-ray cross-correlation from colloidal crystals," J. Appl. Cryst. **49**(Pt 6), 2046–2052 (2016).
14. M. A. Schroer, C. Gutt, and G. Grübel, "Characteristics of angular cross correlations studied by light scattering from two-dimensional microsphere films," Phys. Rev. E Stat. Nonlin. Soft Matter Phys. **90**(1), 012309 (2014).
15. T. Latychevskaia, G. F. Mancini, and F. Carbone, "The role of the coherence in the cross-correlation analysis of diffraction patterns from two-dimensional dense mono-disperse systems," Sci. Rep. **5**, 16573 (2015).
16. G. F. Mancini, T. Latychevskaia, F. Pennacchio, J. Reguera, F. Stellacci, and F. Carbone, "Order/Disorder Dynamics in a Dodecanethiol-Capped Gold Nanoparticles Supracrystal by Small-Angle Ultrafast Electron Diffraction," Nano Lett. **16**(4), 2705–2713 (2016).
17. J. Rajeswari, P. Huang, G. F. Mancini, Y. Murooka, T. Latychevskaia, D. McGrouther, M. Cantoni, E. Baldini, J. S. White, A. Magrez, T. Giamarchi, H. M. Rønnow, and F. Carbone, "Filming the formation and fluctuation of skyrmion domains by cryo-Lorentz transmission electron microscopy," Proc. Natl. Acad. Sci. U.S.A. **112**(46), 14212–14217 (2015).
18. A. Rundquist, C. G. Durfee 3rd, Z. Chang, C. Herne, S. Backus, M. M. Murnane, and H. C. Kapteyn, "Phase-Matched Generation of Coherent Soft X-rays," Science **280**(5368), 1412–1415 (1998).
19. R. A. Bartels, A. Paul, H. Green, H. C. Kapteyn, M. M. Murnane, S. Backus, I. P. Christov, Y. Liu, D. Attwood, and C. Jacobsen, "Generation of Spatially Coherent Light at Extreme Ultraviolet Wavelengths," Science **297**(5580), 376–378 (2002).
20. A. McPherson, G. Gibson, H. Jara, U. Johann, T. S. Luk, I. A. McIntyre, K. Boyer, and C. K. Rhodes, "Studies of multiphoton production of vacuum-ultraviolet radiation in the rare gases," J. Opt. Soc. Am. B **4**, 595 (1987).
21. P. B. Corkum, "Plasma Perspective on Strong Field Multiphoton Ionization," Phys. Rev. Lett. **71**(13), 1994–1997 (1993).
22. X. Zhang, A. R. Libertun, A. Paul, E. Gagnon, S. Backus, I. P. Christov, M. M. Murnane, H. C. Kapteyn, R. A. Bartels, Y. Liu, and D. T. Attwood, "Highly coherent light at 13 nm generated by use of quasi-phase-matched high-harmonic generation," Opt. Lett. **29**(12), 1357–1359 (2004).
23. H. C. Kapteyn, M. M. Murnane, and I. P. Christov, "Extreme nonlinear optics: Coherent x-rays from lasers," Phys. Today **58**, 39–46 (2005).
24. F. Krausz and M. Ivanov, "Attosecond physics," Rev. Mod. Phys. **81**, 163–234 (2009).
25. Z. Tao, C. Chen, T. Szilvási, M. Keller, M. Mavrikakis, H. Kapteyn, and M. Murnane, "Direct time-domain observation of attosecond final-state lifetimes in photoemission from solids," Science **353**(6294), 62–67 (2016).
26. C. Chen, Z. Tao, A. Carr, P. Matyba, T. Szilvási, S. Emmerich, M. Piecuch, M. Keller, D. Zusin, S. Eich, M. Rollinger, W. You, S. Mathias, U. Thumm, M. Mavrikakis, M. Aeschlimann, P. M. Oppeneer, H. Kapteyn, and M. Murnane, "Distinguishing attosecond electron-electron scattering and screening in transition metals," Proc. Natl. Acad. Sci. U.S.A. **114**(27), E5300–E5307 (2017).
27. D. Sayre, "Some implications of a theorem due to Shannon," Acta Crystallogr. **5**, 843 (1952).
28. J. Miao, D. Sayre, and H. N. Chapman, "Phase retrieval from the magnitude of the Fourier transforms of

Optics EXPRESS

nonperiodic objects," J. Opt. Soc. Am. A **15**, 1662 (1998).
29. J. R. Fienup, "Reconstruction of an object from the modulus of its Fourier transform," Opt. Lett. **3**(1), 27–29 (1978).
30. J. Gulden, O. M. Yefanov, A. P. Mancuso, R. Dronyak, A. Singer, V. Bernátová, A. Burkhardt, O. Polozhentsev, A. Soldatov, M. Sprung, and I. A. Vartanyants, "Three-dimensional structure of a single colloidal crystal grain studied by coherent x-ray diffraction," Opt. Express **20**(4), 4039–4049 (2012).
31. A. G. Shabalin, J.-M. Meijer, R. Dronyak, O. M. Yefanov, A. Singer, R. P. Kurta, U. Lorenz, O. Y. Gorobtsov, D. Dzhigaev, S. Kalbfleisch, J. Gulden, A. V. Zozulya, M. Sprung, A. V. Petukhov, and I. A. Vartanyants, "Revealing Three-Dimensional Structure of an Individual Colloidal Crystal Grain by Coherent X-Ray Diffractive Imaging," Phys. Rev. Lett. **117**(13), 138002 (2016).
32. S. Lazarev, Il. Besedin, A. V. Zozulya, J.-M. Meijer, D. Dzhigaev, and O. Y. Gorobtsov, R. P. Kurta, M. Rose, A. G. Shabalin, E. A. Sulyanova, I. A. Zaluzhnyy, A. P. Menushenkov, M. Sprung, A. V. Petukhov, and I. A. Vartanyants,"Ptychographic X-Ray Imaging of Colloidal Crystals," Small **14**, 1–8 (2018).
33. K. Ba Dinh, A. X. P. Ong, H. Vu Le, C. A. Henderson, C. Van Vuong, P. Hannaford, T. A. Smith, and L. Van Dao, "Coherent diffractive imaging of single layer microspheres," J. Appl. Phys. **117**, 163102 (2015).
34. D. F. Gardner, M. Tanksalvala, E. R. Shanblatt, X. Zhang, B. R. Galloway, C. L. Porter, R. Karl, Jr., C. Bevis, D. E. Adams, H. C. Kapteyn, M. M. Murnane, and G. F. Mancini, "Subwavelength coherent imaging of periodic samples using a 13.5 nm tabletop high-harmonic light source," Nat. Photonics **11**, 259–263 (2017).
35. CXRO, http://www.cxro.lbl.gov/.
36. N. J. A. Sloane, "Kepler' s conjecture confirmed," Nature **395**, 435–436 (1998).
37. J.-M. Meijer, A. Shabalin, R. Dronyak, O. M. Yefanov, A. Singer, R. P. Kurta, U. Lorenz, O. Gorobstov, D. Dzhigaev, J. Gulden, D. V. Byelov, A. V. Zozulya, M. Sprung, I. A. Vartanyantsb, and A. V. Petukhova, "Double hexagonal close-packed structure revealed in a single colloidal crystal grain by Bragg rod analysis," J. Appl. Cryst. **47**, 1199–1204 (2014).
38. T. Latychevskaia and H. W. Fink, "Practical algorithms for simulation and reconstruction of digital in-line holograms," Appl. Opt. **54**(9), 2424–2434 (2015).
39. R. P. Kurta, J. J. Donatelli, C. H. Yoon, P. Berntsen, J. Bielecki, B. J. Daurer, H. DeMirci, P. Fromme, M. F. Hantke, F. R. N. C. Maia, A. Munke, C. Nettelblad, K. Pande, H. K. N. Reddy, J. A. Sellberg, R. G. Sierra, M. Svenda, G. van der Schot, I. A. Vartanyants, G. J. Williams, P. L. Xavier, A. Aquila, P. H. Zwart, and A. P. Mancuso, "Correlations in Scattered X-Ray Laser Pulses Reveal Nanoscale Structural Features of Viruses," Phys. Rev. Lett. **119**(15), 158102 (2017).
40. A. M. Maiden and J. M. Rodenburg, "An improved ptychographical phase retrieval algorithm for diffractive imaging," Ultramicroscopy **109**(10), 1256–1262 (2009).
41. A. Maiden, D. Johnson, and P. Li, "Further improvements to the ptychographical iterative engine," Optica **4**, 736 (2017).
42. P. Thibault, M. Dierolf, A. Menzel, O. Bunk, C. David, and F. Pfeiffer, "High-Resolution Scanning x-ray Diffraction Microscopy," Science **321**(5887), 379–382 (2008).
43. P. Thibault, M. Dierolf, O. Bunk, A. Menzel, and F. Pfeiffer, "Probe retrieval in ptychographic coherent diffractive imaging," Ultramicroscopy **109**(4), 338–343 (2009).
44. M. Seaberg, B. Zhang, D. Gardner, E. Shanblatt, M. Murnane, H. Kapteyn, and D. Adams, "Tabletop Nanometer Extreme Ultraviolet Imaging in an Extended Reflection Mode using Coherent Fresnel Ptychography," Optica **1**, 39–44 (2014).
45. F. Zhang, I. Peterson, J. Vila-Comamala, A. Diaz, F. Berenguer, R. Bean, B. Chen, A. Menzel, I. K. Robinson, and J. M. Rodenburg, "Translation position determination in ptychographic coherent diffraction imaging," Opt. Express **21**(11), 13592–13606 (2013).
46. E. Turgut, C. La-o-Vorakiat, J. M. Shaw, P. Grychtol, H. T. Nembach, D. Rudolf, R. Adam, M. Aeschlimann, C. M. Schneider, T. J. Silva, M. M. Murnane, H. C. Kapteyn, and S. Mathias, "Controlling the competition between optically induced ultrafast spin-flip scattering and spin transport in magnetic multilayers," Phys. Rev. Lett. **110**(19), 197201 (2013).
47. S. Mathias, C. La-O-Vorakiat, P. Grychtol, P. Granitzka, E. Turgut, J. M. Shaw, R. Adam, H. T. Nembach, M. E. Siemens, S. Eich, C. M. Schneider, T. J. Silva, M. Aeschlimann, M. M. Murnane, H. C. Kapteyn, and H. C. Kapteyn, "Probing the timescale of the exchange interaction in a ferromagnetic alloy," Proc. Natl. Acad. Sci. U.S.A. **109**(13), 4792–4797 (2012).
48. J. N. Hernandez-Charpak, K. M. Hoogeboom-Pot, Q. Li, T. D. Frazer, J. L. Knobloch, M. Tripp, S. W. King, E. H. Anderson, W. Chao, M. M. Murnane, H. C. Kapteyn, and D. Nardi, "Full Characterization of the Mechanical Properties of 11-50 nm Ultrathin Films: Influence of Network Connectivity on the Poisson's Ratio," Nano Lett. **17**(4), 2178–2183 (2017).
49. K. M. Hoogeboom-Pot, J. N. Hernandez-Charpak, X. Gu, T. D. Frazer, E. H. Anderson, W. Chao, R. W. Falcone, R. Yang, M. M. Murnane, H. C. Kapteyn, and D. Nardi, "A new regime of nanoscale thermal transport: Collective diffusion increases dissipation efficiency," Proc. Natl. Acad. Sci. U.S.A. **112**(16), 4846–4851 (2015).
50. R. M. Karl, G. F. Mancini, D. Gardner, E. Shanblatt, C. Bevis, J. Knobloch, T. Frazer, J. N. Hernandez-Charpak, B. Abad Mayor, E. Shanblatt, M. Tanksalvala, C. Porter, D. Adams, H. Kapteyn and M. M. Murnane, "Stroboscopic Imaging of Acoustic Waves in Nanostructures using Tabletop High Harmonics," Comput. Opt. Sens. Imaging Postdeadline paper **JTh5C.8** (2017).

Optics EXPRESS

1. Introduction

Colloidal crystals ordered in three dimensions form an important class of materials with a diverse range of magnetic, electronic, transport properties [1] with potential applications in nanoelectronics, thermoelectrics, photovoltaics, and nano-enhanced therapies [2–7]. These approaches promise functional materials that go beyond what is possible by simply changing the alloy or multilayer composition of nature-given materials. However, the design of such materials relies critically on the availability of accurate predictive characterization tools and models of how function and mechanical performance are related to nano-to-meso-scale structures [2]. To unravel the local structural properties of colloidal crystals, coherent X-ray scattering and diffractive imaging are important tools [8].

Structural retrieval methods based on computation of the angular cross-correlation function (CCF) from coherent scattering patterns [9,10] have been successfully applied to glassy systems of polymethylmethacrylate spheres [11–13] using hard X-rays from synchrotron facilities, making it possible to extract information on local symmetries in heterogeneous structures. Small-angle scattering combined with angular cross-correlation analysis made it possible to obtain insight into orientational order heterogeneities in densely packed films of silica spheres of different sizes [14]. Recently, a CCF analysis was applied to ultrafast small-angle electron diffraction [15] to probe the ordered arrangement of ligands in a two-dimensional supracrystal of dodecanethiol-capped gold nanoparticles [16], and clarified the microscopic order/disorder dynamics that governs light-induced thermal evolution in such systems. Finally, a CCF analysis from diffraction patterns in a Transmission Electron Microscope (TEM) was used to unravel the structural details with which the helical-to-skyrmion magnetic phase transition occurs in Cu_2OSeO_3, enabling the study of order/disorder correlation in protected magnetic topologies [17].

Extreme ultraviolet (EUV) light from compact High-Harmonic Generation (HHG) sources has unique capabilities for imaging nanomaterials due to its intrinsic chemical, elemental, and spin specificity. Moreover, HHG exhibits very high spatial and temporal coherence, when implemented in a phase matched geometry [18–26]. The high spatial coherence of the HHG beam also makes it possible to combine tabletop coherent small-angle scattering with full-field coherent diffractive imaging (CDI). In CDI, a finite object (sample) is illuminated with a coherent beam; if the far-field diffraction pattern collected at the detector is adequately sampled with respect to the spatial Nyquist frequency [27,28] the phases of the scattered amplitudes can be recovered computationally by an iterative algorithm [29]. Reconstruction of an image of the sample is achieved by computationally propagating the diffracted light to the sample plane. CDI provides a comprehensive and definitive characterization of how light interacts with the sample because the image contains both amplitude and phase information, fully capturing the influence of both material and topographical composition.

Coherent diffractive imaging with hard X-rays from synchrotron sources have recently demonstrated the possibility to image the three-dimensional structure of single colloidal crystal grains [30,31] and enabled two-dimensional microscopy of colloidal crystals with relatively large (418 nm in diameter) nanosphere size [32]. Past work used EUV HHG CDI at a wavelength of 30nm to record scatter patterns from a sparse region of large 2μm core-size silica spheres [33], and achieved a spatial resolution between 250nm and 440nm. However, to date, full-field, quantitative EUV coherent scattering and imaging of close-packed nanosphere multilayers still poses a challenge for a wide range of colloidal crystals, with dimensions ranging from 10nm to 200nm.

In this work, we demonstrate small-angle Bragg scattering from nanostructured materials using a tabletop-scale microscope illuminated by coherent HHG beams, to reveal important information about the local order of silica colloidal crystal grains that are separated by grain boundaries and discontinuities. We also implement full-field quantitative ptychographic coherent imaging to visualize the extended structure of a silica close-packed colloidal crystal multilayer [1], with thickness information encoded in the phase. The high spatial coherence

Optics EXPRESS

and short wavelength (13.5nm) of high harmonic beams, combined with advances in coherent imaging techniques [34] allows us to obtain images with amplitude and phase contrast from near-periodic extended self-assemblies of multilayered silica nanosphere lattices, quantitatively and nondestructively, with a spatial resolution better than 20nm. We achieve excellent agreement between the nanosphere size extracted from scanning electron microscope (SEM) images (123 ± 3nm) and the estimated sphere thickness from the phase reconstruction (124nm ± 1nm). These combined techniques allow us to simultaneously characterize the sphere size, the distribution and level of crystallinity within a single colloidal crystal grain, as well as to probe the arrangement of nearest-neighbor grains. Hence, in a single tabletop-scale EUV microscope, we provide a complete structural characterization of a colloidal crystal of silica nanospheres, with high quantitative accuracy over a broad range of length scales.

In the future, by harnessing the high time resolution of tabletop high harmonics, this technique can be extended to dynamically image the 3D electronic, magnetic, and transport properties of functional nanosystems.

2. Experimental setup

Silica colloidal crystals were prepared by dropcasting monodispersed silica nanospheres with 123 ± 3nm core diameter onto 30nm thick silicon nitride membranes. The sample was then imaged in a scanning electron microscope at a 2.0keV electron energy, Fig. 1 (inset). The sample is composed of three distinct regions characterized by different nanosphere distributions: (left) a sparse aggregate of randomly distributed silica nanospheres, (center) a monolayer of close-packed spheres distributed in grains and characterized by grain boundaries and discontinuities, and (right) a three-dimensional multi-layered colloidal crystal. A high-definition, full-field SEM image of the sample is available in the Appendix A.

The sample was investigated using tabletop-scale 13.5nm high harmonic source driven by a 20fs, 2mJ, 3kHz, Ti:Sapphire laser centered at 785nm (KMLabs Dragon). Bright, phase matched, spatially-coherent HHG beams at a wavelength of 13.5nm were produced in a 150μm diameter waveguide filled with He gas at a pressure of 575Torr. The residual laser light was rejected using a pair of ZrO_2-coated Si mirrors placed near Brewster's angle, followed by a 400nm Zr foil. A single harmonic at a wavelength of 13.5nm was then selected using a pair of Si/Mo multilayer mirrors (CXRO [35]). In our experimental apparatus [34] the first flat mirror, 2.54cm diameter, is used to steer the beam onto a second curved mirror with 100mm radius-of-curvature, which gently focused the 13.5nm beam onto the colloidal crystal sample. Slight astigmatism in the focus of the beam was observed due to the non-zero angle-of-incidence on the curved mirror. For this reason, the sample was placed between the horizontal and vertical foci at the circle-of-least confusion, which was measured using a knife-edge method to be approximately 5μm in diameter. The camera, (Andor iKon, 2048 by 2048 square pixels, side 13.5μm length) was placed 18.3mm away from the sample. A schematic layout of the experiment is provided in Fig. 1.

Optics EXPRESS

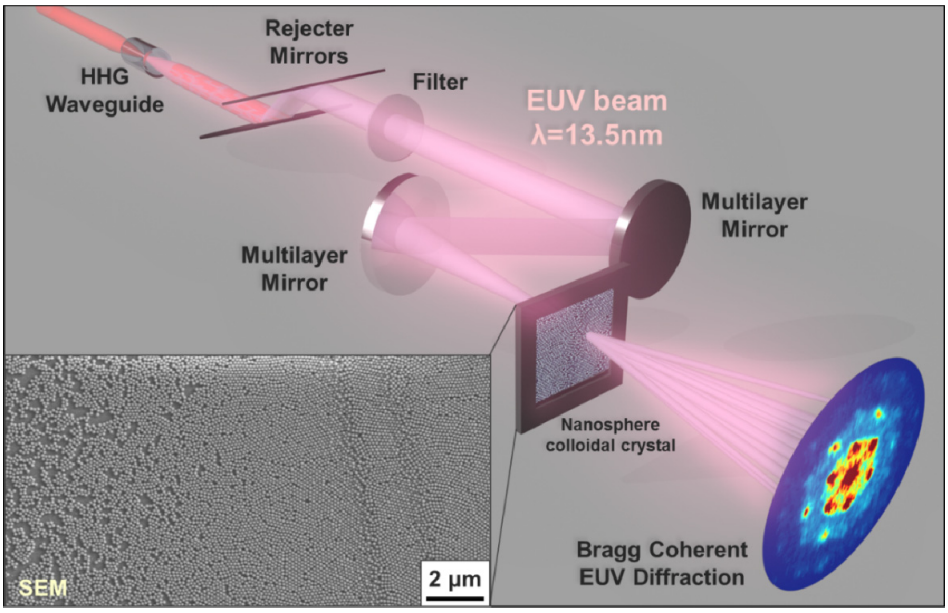

Fig. 1. X-ray scattering and microscopy of a silica nanosphere colloidal crystal using 13.5nm extreme ultraviolet beams from a tabletop high-harmonic source. Bright, phase matched, spatially coherent HHG beams at a wavelength of 13.5nm are produced in a He-filled waveguide. Multilayer mirrors are used to select and focus a single harmonic onto the nanosphere colloidal crystal sample. The light scattered from the sample is collected on an EUV sensitive charged-coupled device (CCD). CDI images of the sample are obtained by raster scanning the sample across the beam at the focus, and the diffraction from each position is collected. The image at the sample plane and in the inset is a scanning electron microscope (SEM) image of the sample.

3. Tabletop EUV scattering

Coherent EUV diffraction patterns were collected from two distinct regions of the sample (left and right regions in the inset of Fig. 1). The sample was aligned perpendicular to the beam, in transmission geometry. The diffraction patterns were collected at room temperature by acquiring a series of 20 frames with an exposure time of 12 sec for the pattern of Fig. 2(a) and 3.5 sec for Fig. 2(d), with 1x1 binning on the camera at 1MHz pixel readout rate. In these experimental conditions, and the overall fluence of the 13.5nm light impinging on the each sample region was calculated to be less than 4μJ/cm^2, thus allowing for non-destructive probing of the structure of the colloidal crystal. Note that recent progress (*i.e.*, after these experiments were carried out) has increased the 13.5nm flux by a factor of 20, allowing for much reduced sample exposure times. The resulting diffraction patterns, obtained by summing up all frames in a series, are reported in Fig. 2(a, d).

In the diffraction pattern of Fig. 2(a), several orders of Bragg peaks are visible due to the long-range order of the colloidal crystal in this region. Colloidal self-assemblies are known to organize into close-packed hexagonal layers that can either lead to the hexagonal close-packed (h.c.p.) or face-centred cubic (f.c.c.) colloidal crystals [36]. These systems are often found to form a random sequence of both stacking types, yielding a random close-packed structure, due to the low difference in free-energy between the two structures [37].

Optics EXPRESS

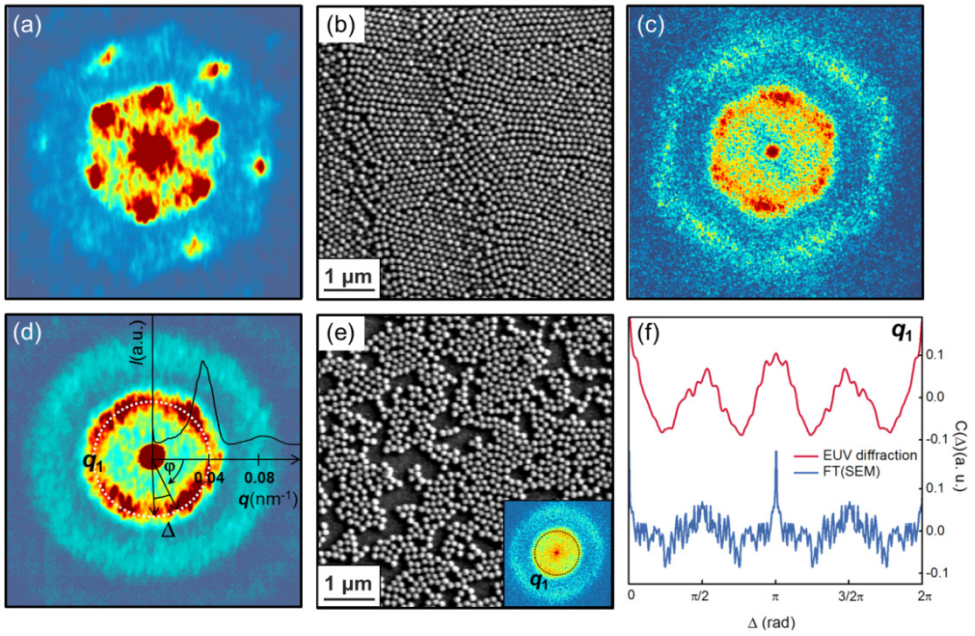

Fig. 2. Coherent EUV scattering from silica nanosphere lattices of different symmetry. (a, d) EUV Bragg diffraction of different sample regions and (d) illustration of angular cross-correlation. The diffraction patterns are plotted on a logarithmic scale. (b, e) Scanning Electron Microscopy images of the sample probed with EUV Bragg coherent diffraction. (c and inset of e) Simulations obtained as the squared amplitude of the Fourier transform from (b) and (e), respectively. (f) Compared CCFs between (d) the EUV coherent pattern from the sample and (inset of e) the simulation from a region of the SEM image. The four-fold periodicity in both curves show a qualitative agreement in the determination of the lattice symmetry for that sample region.

To confirm that the experimental EUV coherent diffraction pattern, Fig. 2(a), originates from the multi-layered region of the nanospheres in the colloidal crystal, we carried out a series of simulations starting from the SEM image of the sample. We selected an area of the SEM image corresponding to the sample area illuminated by the EUV beam (5μm spot-size), and characterized by a multilayered arrangement of close-packed nanospheres. Figure 2(b) shows the selected area of the SEM image of the sample used for the simulation. The corresponding diffraction pattern, Fig. 2(c), was simulated as the squared amplitude of the Fourier Transform (FT) of the SEM image. Artifacts in all two-dimensional Fourier transforms, associated with image re-scaling, were avoided by converting the image to a binary (black and white) image, followed by multiplication with an apodizing cosine function to smooth the edges of the images and remove the scale-bar [38]. The two-dimensional Fourier transform was then normalized to the number of nanoparticles detected in the corresponding SEM image. The diffraction pattern thus obtained shows agreement in both orientational order and symmetry to the experimental pattern of Fig. 2(a).

The Debye-Scherrer rings typical of a more-disordered region of the silica colloidal crystal were detected in the same sample, as shown in Fig. 2(d). The analysis of this diffraction pattern was carried out calculating the radial integrated intensity distribution $I(q)=\frac{1}{2\pi}\int I(q,\varphi)d\varphi$ of the scattered intensity at the detector. The resulting integrated intensity profile is reported with the black solid line in Fig. 2(d), overlaid to the diffraction pattern. From this analysis we estimate that, in this region of the colloidal crystal, silica nanospheres have a characteristic interparticle distance d_1 = 149 ± 2nm (q_1 = 0.0415nm^{-1}). This value, compared to the nanosphere diameter estimated from SEM images (123 ± 3nm),

Optics EXPRESS

suggests that assemblies of spheres in this region are characterized by a sparse distribution. For the simulations we then selected an area of the SEM image of the sample characterized by a sparse arrangement of nanospheres, Fig. 2(e), and computed the FT, reported in Fig. 2(e, inset). The procedure for this simulation is identical to the one adopted for the results in Fig. 2(b, c).

The Bragg pattern obtained with coherent EUV light contains information in its speckle that is associated to local arrangement and the symmetry of nanospheres in colloidal assemblies. Methods based on the computation of angular cross-correlation functions [9–13,39] (CCF) give access to order/disorder correlations in such systems. A schematic illustration of the CCF, at the scattering vector q_1, is provided in Fig. 2(d). With $I(q_1,\varphi)$ being the diffracted intensity at the scattering vector q_1 and the azimuthal angle φ, and Δ the shift between the two angles, the normalized CCF can be calculated as:

$$C_{norm}(\Delta)=\frac{\langle I(q_1,\varphi)I(q_1,\varphi+\Delta)\rangle_\varphi-\langle I(q_1,\varphi)\rangle^2_\varphi}{\langle I(q_1,\varphi)\rangle^2_\varphi}. \quad (1)$$

The normalized CCF can also be calculated from the the one-dimensional FT of $I(q_1,\varphi)$ over the azimuthal coordinate φ, as [15,16]:

$$C(\Delta)=\langle I(q_1,\varphi)I(q_1,\varphi+\Delta)\rangle_\varphi=\mathrm{Re}\left(F_\varphi^{-1}\left(\left|F_\varphi\{I(q_1,\varphi)\}\right|^2\right)\right). \quad (2)$$

The investigation of the local symmetry of the nanosphere assemblies in both the experimental pattern, Fig. 2(d), and in the simulation, Fig. 2(e, inset), is carried out at the scattering vector q_1. The resulting CCFs are displayed in Fig. 2(f), with experimental data in red and the simulation in blue. The CCF analysis demonstrates that experimental data and simulation are in qualitative agreement. The area of the sample illuminated by the EUV beam is indeed characterized by a sparse distribution of nanospheres, as suggested by the integrated intensity profile analysis.

Furthermore, the four-fold periodicity of the CCFs for both experimental and simulated diffraction patterns suggest that within the overall sparse arrangement, the silica nanospheres are locally distributed in small patches characterized by a preferential four-fold symmetry. Hence, this method allows us to characterize the local structural order of the colloidal sample by comparing experimental data to simulations that are based on the real-space image of the sample itself, yielding insights in the microscopic structure of these colloidal systems.

4. Coherent EUV small-angle scattering

As discussed above, computation of angular cross-correlation functions is effective in determining the average, local arrangement of nanoparticles within neighbor grains. In combination to small-angle scattering, CCFs also gave insights in the local arrangements of grains and their annealing processes [16]. In our experiment, the angular cross-correlation analysis at small-angle scattering vectors (close to the DC) reveals important information on the arrangement of grains containing several nanospheres. To make sure we could probe a few neighboring grains of average center-center distance ≈1μm, we increased the EUV beam size at the focus to 15μm, and illuminated a monolayer region of close-packed spheres distributed in grains and characterized by grain boundaries and discontinuities, Fig. 3(b). The sample was placed 15.1mm away from the detector. We remark that small-angle EUV scattering experiments were carried out with the same experimental setup described in Section 2, changing only the EUV spot size at the sample plane and the sample-CCD distance.

Optics EXPRESS

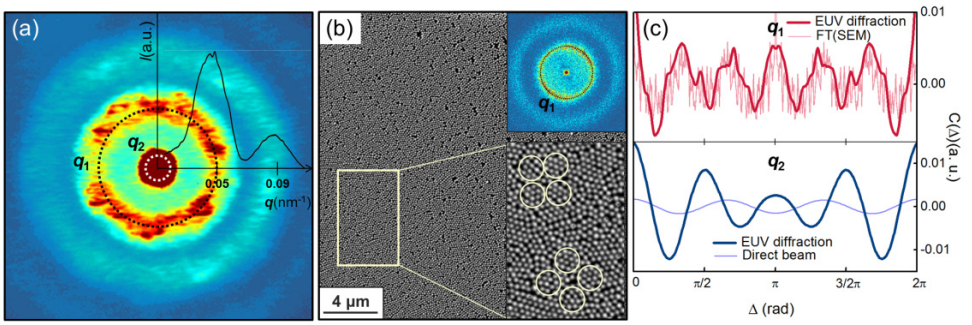

Fig. 3. Visualization of grain symmetry using small-angle coherent EUV scattering. (a) Coherent diffraction pattern of a silica nanosphere monolayer obtained with an EUV beam size of 15µm. The diffraction pattern is plotted on a logarithmic scale. (b) SEM image of the sample. Insets: Top: Simulation obtained as the squared amplitude of the FT of the image in (b). Bottom: Four-fold grain arrangements are highlighted in white in the zoomed region of the SEM image. (c) Top: Cross- correlation analysis at q_1, showing the hexagonal arrangement of spheres within randomly distributed grains. Red trace: experimental cross-correlation function. Pink trace: CCF from the simulation. Bottom: The angular cross-correlation analysis applied at q_2 reveals the presence of a four-fold arrangement of the grains in the colloidal crystal (blue trace), as opposed to the trace obtained without the sample (light blue trace).

The diffraction pattern, Fig. 3(a), was collected at room temperature, in a transmission geometry, by acquiring a series of 30 frames with an exposure time of 9 sec with 1x1 binning on the camera at 1MHz pixel readout rate. The FT of the SEM image was obtained following the same procedure as in Fig. 2, and it is shown in Fig. 3(b, upper inset).

The CCF calculated from the EUV diffraction pattern at $q_1 = 0.05\text{nm}^{-1}$ reveals a local hexagonal arrangement of nanospheres within grains (upper panel of Fig. 3(c), red trace). This 6-fold symmetry is confirmed by the CCF from the FT of the SEM image of the nanosphere monolayer (upper panel of Fig. 3(c), pink trace). Furthermore, the analysis of the integrated radial intensity from the experimental pattern, Fig. 3(a) shows that, in this region of the colloidal crystal, nanospheres form crystallographic-like planes with average interplanar distance $d_1 = 125 \pm 2$nm. This value is in excellent agreement with the data obtained for the nanosphere diameter from SEM (123 ± 3nm).

To retrieve the symmetry of a few nearest-neighbor grains of average center-center size ≈1µm, the CCF was calculated at $q_2 \approx 0.006\text{nm}^{-1}$. In Fig. 3(c, bottom) we report in blue the resulting CCF for the nanosphere monolayer. We also report the data without the sample (light blue trace) for comparison. The Fourier components as well as the image of the beam are reported in the Appendix B. The modulation of the CCF for the sample indicates that in this portion of the monolayer, grains that include several nanospheres have an average nearest-neighbour arrangement that is preferentially four-fold. In Fig. 3(b, lower inset) we display the local four-fold arrangement of the grains in a zoomed region of the SEM image for clarity. With this approach, we demonstrate that we can fully characterize – in a single measurement – the average nanosphere distribution within grains, their average interparticle distance, and the nearest neighbor grains arrangement in the colloidal crystal. Thus, we show that this technique provides a valuable tool for the characterization of a broad variety of nano-engineered materials.

Optics EXPRESS

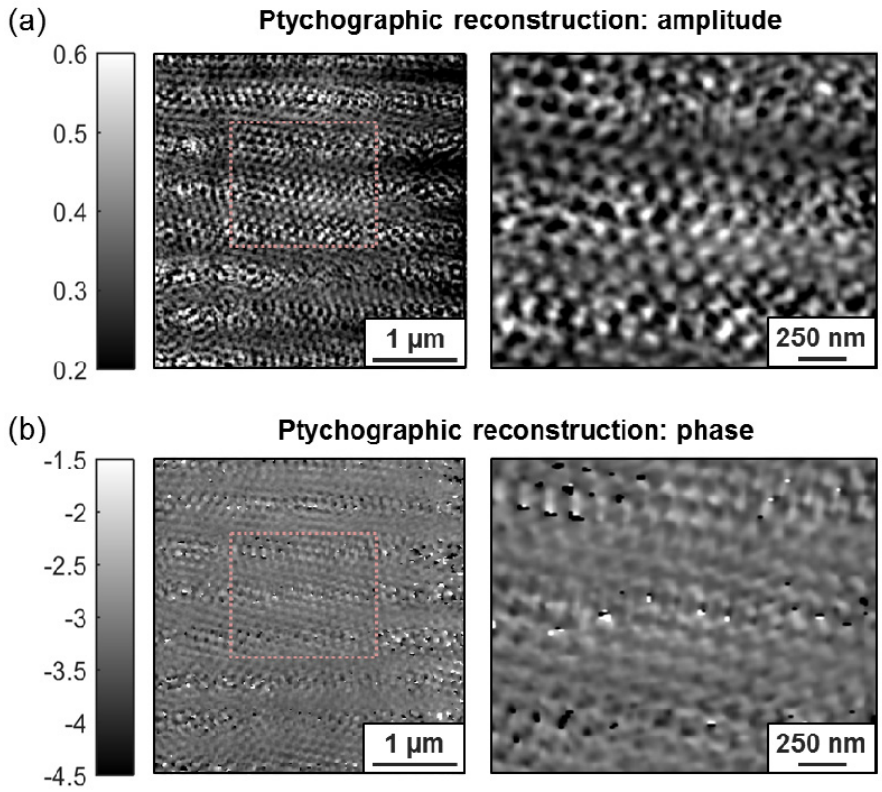

Fig. 4. Quantitative, non-destructive imaging of a near-periodic 3D silica nanosphere colloidal crystal. EUV ptychographic CDI of a self-assembled nanosphere multilayer. (a) Reconstructed quantitative amplitude and (b) phase. Left: large field of view reconstructions. The scale bars are 1μm. The diffraction pattern from the multi-layered region, at the center of the ptychography scan grid, is reported in Fig. 2(a). Right: zoomed in reconstructed amplitude and phase. The scale bars are 250nm.

5. Coherent diffractive imaging

Recently, a powerful approach to CDI called ptychography [40–42] has significantly increased the fidelity, speed and robustness of coherent imaging. In ptychography, multiple diffraction patterns are collected by scanning the illuminating beam across the sample, such that each scan position overlaps with adjacent positions [40–42]. This overlap provides the ptychography algorithm with a large amount of redundant information, so that it can solve for not only the sample, but also the illumination function. Recently, we used a novel technique called Modulus Enforced Probe (MEP) to enable high-fidelity ptychographic diffractive imaging of periodic objects, demonstrating sub-wavelength spatial resolution [34].

The nanosphere sample was imaged using 13.5nm high harmonic beams in a ptychographic CDI microscope at room temperature. The sample was scanned in the focus of the EUV beam in a rectilinear pattern, with 81 (9 *x* 9) positions, nominally separated by 1.2μm between adjacent positions. At each scan position, 2 frames were acquired with an exposure time of 4 sec, with 1x1 binning on the camera at 1MHz pixel readout rate (as noted above, we have recently achieved a x20 decrease in exposure times). A random offset of ± 30% of the step size was added to each scan position to prevent the scanning grid from introducing periodic artifacts [43,44]. The EUV beam at the focus was measured using a knife-edge method to be approximately 5μm in diameter and placed 18.3mm away from the detector. The diffraction pattern from the multi-layered region, at the center of the scan grid, is reported in Fig. 2(a). The reconstructed image is obtained with the ePIE algorithm [40]

Optics EXPRESS

with Modulus Enforced Probe [34] for a total of 3350 iterations with 750 iterations of a position correction algorithm [45]. The relaxation parameter for the probe was set to 3; for the object it was set to 1. The object was re-initialized to unity on the 50th, 350th, and 1350th iteration.

The ptychographic reconstructions are shown in Fig. 4. Note that the reconstructed images have horizontal regions where the fidelity is reduced; this is because the EUV beam was oblong in shape due to the focusing optics used (see Appendix C) so that it was shorter in the vertical direction than expected. As a result, the required overlap of the beam for ptychographic scanning was not met in some regions of the sample, leading to a lower spatial resolution in striped regions. In the future, a lower step size in the vertical direction could correct this. Nevertheless, in regions where the overlap is good, we retrieve quantitative images that agree with the sample properties measured in the SEM images. The numerical aperture of our diffraction patterns is 0.37, which supports a resolution $\Delta_r = \lambda/2NA$ of 18.2nm.

From the reconstructed images, we can extract the lateral separation of the nanospheres to be 125nm. From the reconstructed phase, and knowing the material composition of the colloidal crystal (silica), we can determine the thickness of silica at each spatial location. Comparing a region at the center of a nanosphere to a region in between nanospheres, we find a phase difference of 0.16rad, which corresponds to a thickness of 124nm, which is in good agreement with the estimated nanosphere size from the SEM images. The precision on the sphere size estimated with this method is ± 1nm. In determining the nanosphere thickness, we considered the contribution from the Fresnel phase, which occurs at the interface of the silica sphere and silicon nitride membrane. In our case, the Fresnel phase from the silica was calculated to be 5.6μrad, and were thus considered negligible. In the phase image, Fig. 4(b), there are regions where the phase appears to wrap; these are locations where the amplitude is reconstructed to be zero, hence the phase assigned at that pixel has no physical meaning.

The amplitude reconstruction, Fig. 4(a), shows quantitatively the spatially dependent transmissivity of the sample. Comparing a high transmission region to a low transmission region, we see that the ratio of the transmissivities is 0.54, which is in agreement with the transmission through 124nm of silica [35]. Furthermore, the values of the transmissivity range from 0.2 to 0.6, which correspond to transmission through 30nm of silicon nitride followed by transmission through 248nm and 124nm of silica, respectively. This indicates that every part of the reconstructed image has propagated through part of a silica nanosphere, thus demonstrating that the imaged region is a multilayer.

6. Conclusions

The combination of small-angle Bragg scattering and angular cross-correlation analysis, with tabletop short wavelength HHG ptychographic imaging, opens up exciting new opportunities for studying nano-to-mesoscopic materials. We presented the first demonstration of small-angle Bragg EUV scattering from nanostructures using a tabletop-scale setup, enabling structural characterization of colloidal crystals of different packing symmetry. By harnessing the high spatial coherence of HHG beams, we also showed that coherent diffractive imaging can be used to directly visualize 2D and 3D colloidal crystal symmetry in real space, with a spatial resolution better than 20nm. Moreover, by harnessing the high coherence of the HHG beam, we showed that coherent diffractive imaging can be used to non-destructively visualize periodically extended self-assemblies of multilayered nanospheres and to retrieve quantitative information about the sample. Since these nanosphere assemblies represent the lattice-texture equivalent of topologically-protected spin-textures such as magnetic bubbles and skyrmions, this approach can also be used to image charge and spin textures, as well as to other nano-scale self-assemblies, with broad impact in material science and nanotechnology. Indeed, the ultrafast temporal resolution of high harmonic sources ($<10^{-15}$ sec) combined with chemical,

Optics EXPRESS

elemental and spin specificity, has already been used to capture the fastest charge and spin dynamics in materials [46–49], and has very recently been extended to dynamic imaging [50] of thermal and acoustic dynamics in nanostructures. In the future, this approach can be extended to 3D structural and dynamic properties of many different types of colloidal crystals, with broad potential impact in material science and nanotechnology.

7. APPENDICES

A. Scanning Electron Microscopy image of the sample

Figure 5 shows a high-definition, full-field SEM image of the sample.

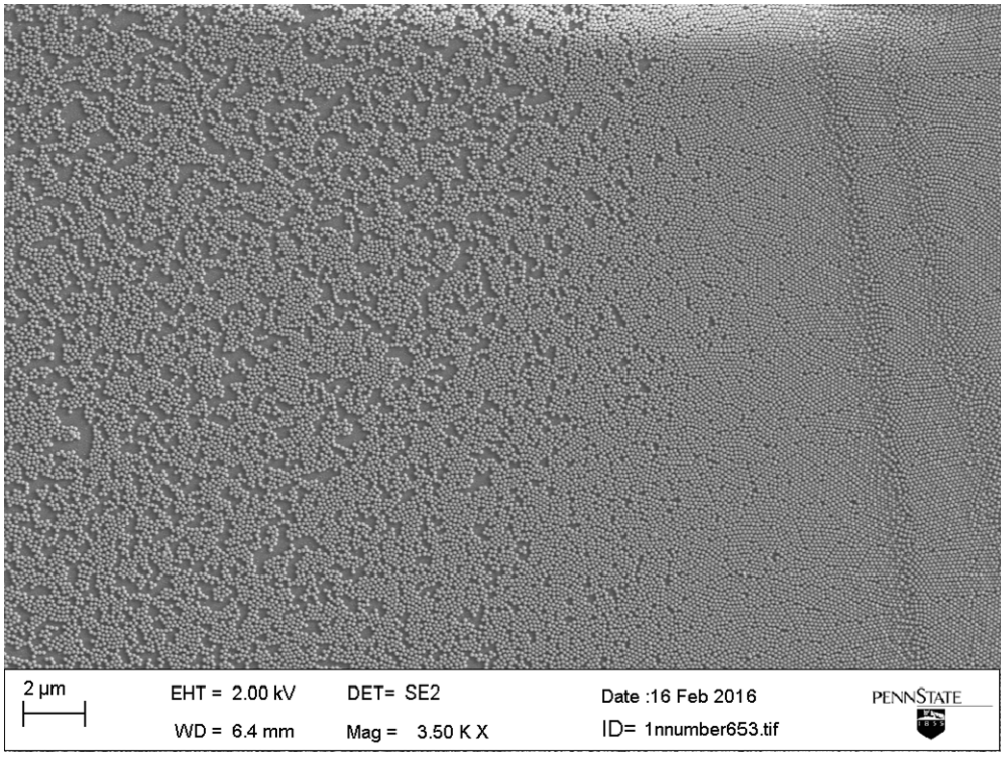

Fig. 5. High-definition, full-field SEM image of the sample. Three regions with different nanosphere distribution are visualized: (left) sparse, (center) close-packed monolayer of silica nanospheres distributed in grains and characterized by grain boundaries and discontinuities, (right) three-dimensional multilayered self-assembly characterized by the presence of multiple close-packed layers.

B. Fourier spectral analysis

Figure 6 shows normalized Fourier spectral components for the sample.

Optics EXPRESS

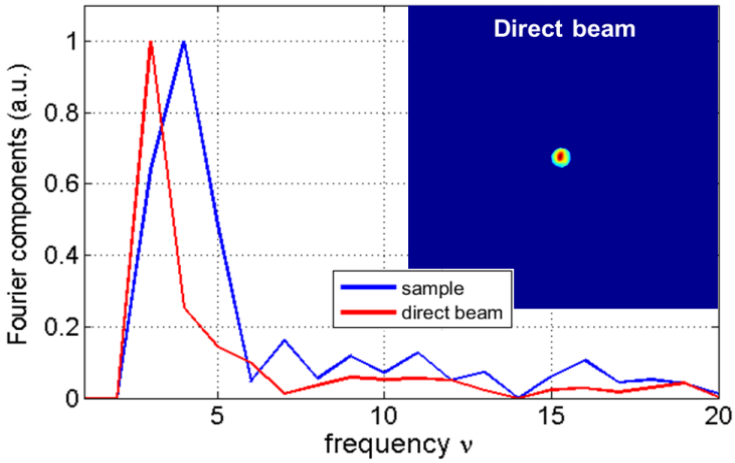

Fig. 6. Normalized Fourier spectral components for the sample (blue) and for the direct beam (red). Inset: direct beam with hard edge applied for ptychographic CDI scans.

C. Probe reconstruction

Figure 7 shows intensity and phase of the EUV illumination at the sample plane.

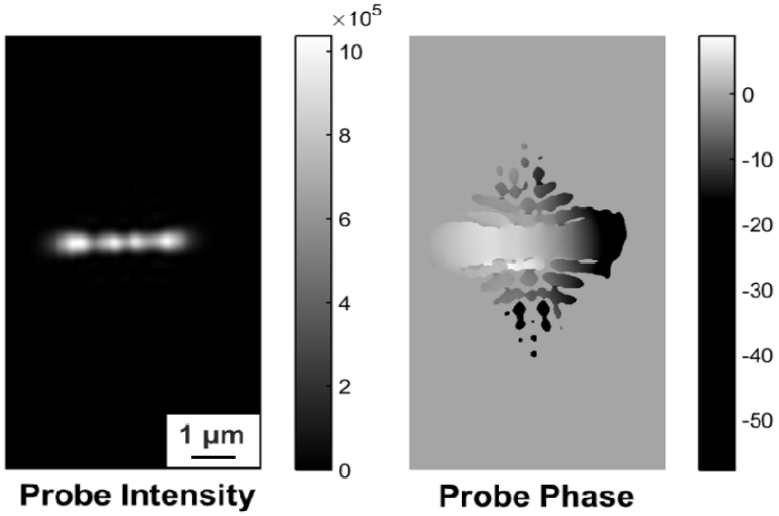

Fig. 7. Intensity (left) and phase (right) of the EUV illumination at the sample plane. The intensity of the illumination is shown in detector counts. The phase is shown in radians. The reconstructed EUV beam has an oblong shape, shorter in the vertical direction than expected.

Author contributions

J.B, H.C.K. and M.M.M. conceived the experiment. G.F.M. collected the data sets, analyzed the data, performed the SEM simulations. R.M.K. performed the reconstructions and data analysis. G.F.M. and D.F.G. characterized the source. J.L.R. and T.E.M. developed the assembly method and J.L.R. prepared the samples. All authors commented on aspects of the experiment, on the results, and on the paper.

Funding

Penn State Center for Nanoscale Science, an NSF-sponsored Materials Science and Engineering Center (DMR-1420620, DARPA PULSE: W31P4Q-13-1-0015); Gordon and

Optics EXPRESS

Betty Moore Foundation's EPiQS Initiative (GBMF: 4538); Swiss National Science Foundation (SNSF) (P2ELP2_158887); NDSEG fellowship; NSF GRFP Fellowship.

Disclosures

MM and HK have a financial interest in KMLabs.